PAPER

Magnetic proximity effect in the two-dimensional ε-Fe$_2$O$_3$/NbSe$_2$ heterojunction

View the article online for updates and enhancements.

Magnetic proximity effect in the two-dimensional ε-Fe$_2$O$_3$/NbSe$_2$ heterojunction

Bingyu Che(车冰玉)[1,2,†], Guojing Hu(胡国静)[1,†], Chao Zhu(朱超)[3], Hui Guo(郭辉)[1,2],
Senhao Lv(吕森浩)[1], Xuanye Liu(刘轩冶)[1,2], Kang Wu(吴康)[1,2], Zhen Zhao(赵振)[1,2],
Lulu Pan(潘禄禄)[1], Ke Zhu(祝轲)[1,2], Qi Qi(齐琦)[1,2], Yechao Han(韩烨超)[1,2], Xiao Lin(林晓)[2],
Zi'an Li(李子安)[4], Chengmin Shen(申承民)[1,2], Lihong Bao(鲍丽宏)[1,2], Zheng Liu(刘政)[3,¶],
Jiadong Zhou(周家东)[5,§], Haitao Yang(杨海涛)[1,2,‡], and Hong-Jun Gao(高鸿钧)[1,2]

[1] *Beijing National Center for Condensed Matter Physics and Institute of Physics, Chinese Academy of Sciences, Beijing 100190, China*
[2] *School of Physical Sciences, University of Chinese Academy of Sciences, Beijing 100190, China*
[3] *School of Materials Science and Engineering, Nanyang Technological University, Singapore*
[4] *School of Physical Science and Technology, Guangxi University, Guangxi 530004, China*
[5] *School of Physics, Beijing Institute of Technology, Beijing 100081, China*

Two-dimensional (2D) magnet/superconductor heterostructures can promote the design of artificial materials for exploring 2D physics and device applications by exotic proximity effects. However, plagued by the low Curie temperature and instability in air, it is hard to realize practical applications for the reported layered magnetic materials at present. In this paper, we developed a space-confined chemical vapor deposition method to synthesize ultrathin air-stable ε-Fe$_2$O$_3$ nanosheets with Curie temperature above 350 K. The ε-Fe$_2$O$_3$/NbSe$_2$ heterojunction was constructed to study the magnetic proximity effect on the superconductivity of the NbSe$_2$ multilayer. The electrical transport results show that the subtle proximity effect can modulate the interfacial spin–orbit interaction while undegrading the superconducting critical parameters. Our work paves the way to construct 2D heterojunctions with ultrathin nonlayered materials and layered van der Waals (vdW) materials for exploring new physical phenomena.

1. Introduction

The exchange interaction in two-dimensional (2D) magnetic heterostructures has become an intriguing research direction due to the potential of breaking the time-reversal symmetry of the originally degenerate band structures. Currently, various 2D materials have been integrated with magnetic materials, such as topological insulators,[1,2] semiconductors[3–6] and superconductors.[7] Among them, 2D magnet/superconductor heterostructures are especially interesting because both systems are closely associated with the alignment of charge spin. Intuitively, superconductivity and ferromagnetism are incompatible. However, curious phenomena arise in magnet–superconductor heterojunctions, including unconventional superconductivity, topological superconductivity, and the modulation of magnetic alignment by Ising superconductivity.[7–11] Therefore, magnet/superconductor junctions offer a great platform to study the fundamental interaction between superconductivity and magnetism. Moreover, they produce significant opportunities to develop spintronics and superconducting spintronic devices.[9]

Intrinsic 2D vdW magnets have been found in Cr, Fe, V, and Mn based materials.[12] Some of the most famous ones such as CrI$_3$, Cr$_2$Ge$_2$Te$_6$, and Fe$_3$GeTe$_2$ have weak ferromagnetic properties.[13–16] Without gate voltage modulation, the Curie temperatures (T_C) of these magnetic 2D vdW materials are far below room temperature, typically, 45 K for monolayer CrI$_3$,[13,14] 30 K for bilayer Cr$_2$Ge$_2$Te$_6$,[15] and 130 K for monolayer Fe$_3$GeTe$_2$.[16] Such low T_C results in the impossible application in the room-temperature device. Although the T_C of Fe$_5$GeTe$_2$ reaches 320 K,[17,18] magnetic 2D vdW materials reported at present are unstable in air, which hinders the exploration of their application. In contrast, non-layered ferrimagnetic iron oxides can maintain magnetic properties up to room temperature and are stable in the ambient environment.[19] However, the study of magnetic proximity in 2D ε-Fe$_2$O$_3$-based devices is still at an embryonic stage.

In this paper, we developed a space-confined chemical vapor deposition (CVD) strategy to synthesize ultrathin ε-

---

Fe$_2$O$_3$ nanosheets with thicknesses down to 3 nm. Ultrathin ε-Fe$_2$O$_3$ nanosheets have room-temperature ferrimagnetic properties and excellent air-stability. ε-Fe$_2$O$_3$/NbSe$_2$ heterojunctions have been constructed by a standard transfer and stacking technique to explore magnetic proximity on superconductivity of NbSe$_2$ multilayers. The result shows that the subtle proximity effect of the ε-Fe$_2$O$_3$ nanosheet can modulate the spin–orbit interaction (SOI) of the NbSe$_2$ multilayer with negligible influence on its superconducting critical parameters. Our work provides a potential platform to study proximity effects in 2D heterojunctions based on ultrathin non-layered materials.

2. Experimental details

2.1. Growth of ε-Fe$_2$O$_3$ nanosheets

A space-confined CVD strategy was used to synthesize ε-Fe$_2$O$_3$ nanosheets. The ε-Fe$_2$O$_3$ nanosheets were grown on the fluorophlogopite mica (Changchun Taiyuan Fluorophlogopite Co., China) substrate. A mixture of anhydrous ferrous chloride (FeCl$_2$) and KCl powder with a mass ratio of about 10:1 was used as the precursor. A small amount of the precursor was put directly between two pieces of freshly cleaved mica (10 mm×10 mm in size). Before heating, the furnace was vacuumed and purged by pure argon to remove the residual oxygen and moisture. Then the furnace was heated to 640 °C in 15 min and held at that temperature for 2 min before cooling down naturally to room temperature, with 100 sccm Ar and 1.5 sccm O$_2$ flowing through the furnace during the whole process. ε-Fe$_2$O$_3$ nanosheets were grown on both pieces of mica substrates.

2.2. Sample characterization

Raman spectra were obtained by HORIBA LabRAM HR Evolution. X-ray photoelectron spectroscopy (XPS) tests were conducted in an ultrahigh vacuum system (VG ESCALAB-5) equipped with XPS. The thicknesses and the magnetic force microscopy (MFM) image of ε-Fe$_2$O$_3$ nanosheets were obtained by Oxford Cypher S atomic force microscope. The HAADF imaging was carried out on JEOL ARM-200F (S)TEM equipped with CEOS CESCOR Cs probe corrector, using a 200 kV acceleration voltage. The convergence semi-angle was set to 27–33 mrad and the collection semi-angle was 60–280 mrad for the image acquisition. Magnetization measurements were carried out by using a vibrating sample magnetometer (MPMS 3, Quantum Design). Both electrical resistance and voltage dependence of current (V–I) data were collected on a Quantum Design physical properties measurement system (PPMS).

3. Results and discussion

As shown in Fig. 1(a), ε-Fe$_2$O$_3$ has a non-symmetric orthorhombic structure, where Fe ions occupying four inequivalent sites are labeled as Fe(1), Fe(2), Fe(3), and Fe(4).[20–22] They are the centers of either an oxygen octahedron or a tetrahedron. The room-temperature ferrimagnetism of ε-Fe$_2$O$_3$ mainly comes from Fe(3) and Fe(4), whose magnetic moments are anti-collinear with different magnitudes, while the magnetic moments of Fe(1) and Fe(2) compensate for each other.[21] ε-Fe$_2$O$_3$ is a rare phase in the iron oxide family, which only exists in the nanoparticle form, not in the bulk form. It was hard to obtain pure ε-Fe$_2$O$_3$ single crystals because the synthetic routes involved phase transition.[22] However, some CVD methods have recently been introduced to synthesize air-stable ε-Fe$_2$O$_3$ nanosheets with thickness above 4 nm.[23–25] Here we developed a space-confined CVD technique to synthesize large non-layered ε-Fe$_2$O$_3$ nanosheets with thinner thicknesses than the reported ones (as described in Section 2). The thinnest thickness of our as-grown hexagonal ε-Fe$_2$O$_3$ nanosheets is down to 3 nm (Figs. 1(b) and 1(c)). The XPS spectrum across an area of 2×0.2 mm^2 confirms that all Fe ions in the nanosheets are Fe^{3+}, with no trace of Fe^{2+} (Fig. 1(d)).[26,27] As shown in Fig. 1(e), the Raman spectrum of ε-Fe$_2$O$_3$ nanosheets has four unique Raman peaks between 100 cm^{-1} and 200 cm^{-1} as hallmarks to verify the ε-Fe$_2$O$_3$ phase, which do not exist in γ-Fe$_2$O$_3$ or α-Fe$_2$O$_3$ phase.[23,28] The Raman mapping result of a typical nanosheet indicates the pure ε-Fe$_2$O$_3$ phase in the whole sample (Fig. 1(f)).

Scanning transmission electron microscopy (STEM) characterization was carried out to get a clearer understanding of the atomic arrangement and quality of the as-synthesized ε-Fe$_2$O$_3$ nanosheets. In the large-area ADF (annular dark field) image of the ε-Fe$_2$O$_3$ nanosheet along the c-axis (Fig. 2(a)), there are no lattice defects across the whole area, indicating the high crystalline quality of the nanosheet. The Fourier transform of the large-area ADF image in Fig. 2(b) shows only one set of spots, which is consistent with the simulated diffraction pattern along the c-axis of the ε-Fe$_2$O$_3$ crystal (Fig. 2(c)). In the zoomed image of the large-area ADF image, a perfect honeycomb lattice composited of spots with different brightness is observed (Fig. 2(d)). The brightness of the spots corresponds to different compositions of the atom columns beneath the sample surface. As the oxygen atoms have less contribution to the ADF signals than the iron atoms, the columns with more iron atoms are much brighter than those with fewer iron atoms. The experimental image matches well with the simulated ADF image (Fig. 2(e)) and the crystalline structure (Fig. 2(f)). The intensity of the experimental signals also agrees with the simulated data in Fig. 2(g), which demonstrates the high quality of the ε-Fe$_2$O$_3$ nanosheets.
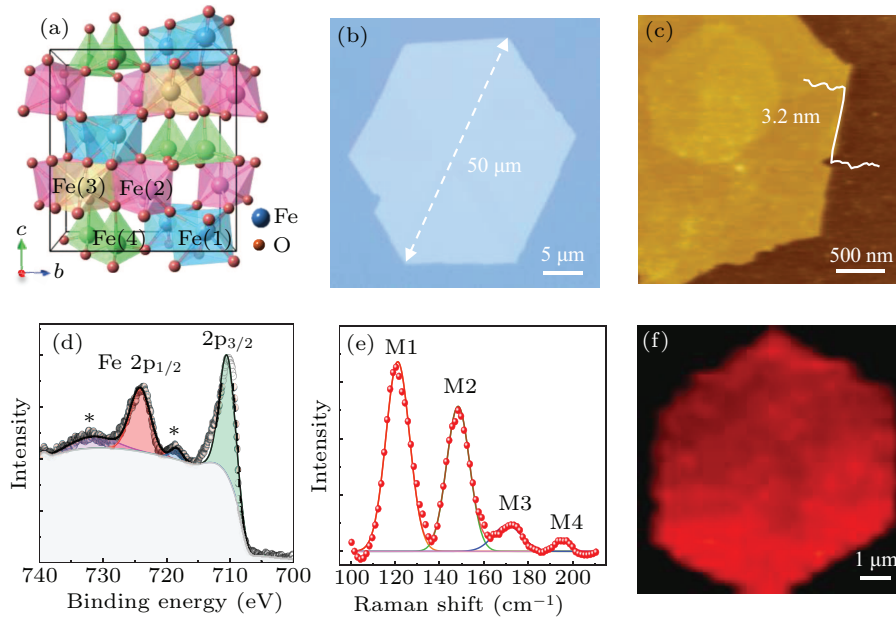
Fig. 1. (a) Crystalline structure of ε-Fe$_2$O$_3$. (b), (c) Optical and AFM images of a typical ε-Fe$_2$O$_3$ nanosheet, showing the lateral size and thickness. (d) XPS of ε-Fe$_2$O$_3$ nanosheets on the mica substrate. The circles and the lines are the experimental and fitting data. (e) Raman spectrum of the ε-Fe$_2$O$_3$ nanosheet. The red dots and the solid lines are the experimental and fitting data. (f) Raman mapping of the ε-Fe$_2$O$_3$ nanosheet, showing the uniform chemical distribution. The sum range is between 100 cm^{-1} and 200 cm^{-1}.
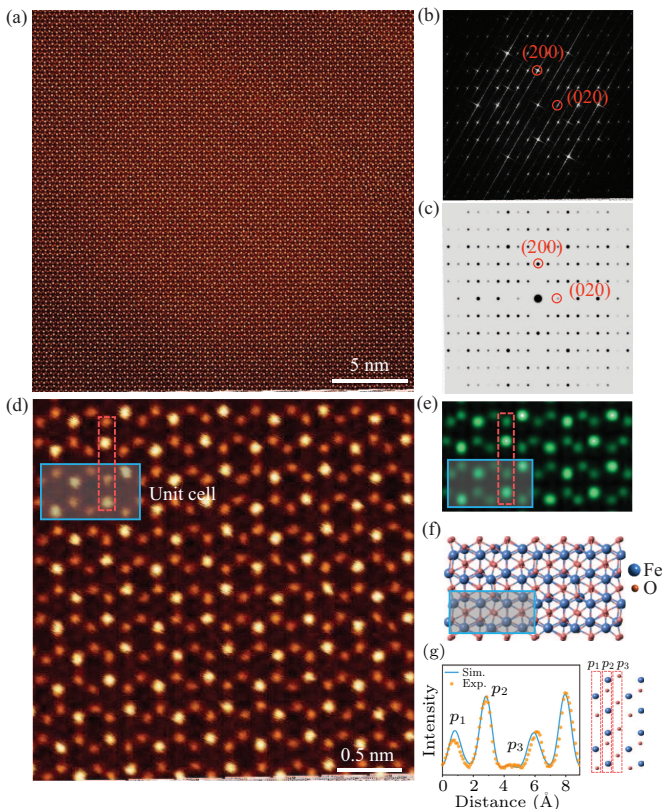
Fig. 2. STEM analysis of the ε-Fe$_2$O$_3$ nanosheet. (a) Large-area ADF-STEM image of the ε-Fe$_2$O$_3$ nanosheet. (b) The Fourier transition pattern of (a). (c) The simulated diffraction pattern of ε-Fe$_2$O$_3$. (d), (e) Zoomed ADF-STEM image of the ε-Fe$_2$O$_3$ nanosheet and its corresponding simulated image. The blue rectangular highlights one unit cell. (f) The crystalline structure along the c-axis of ε-Fe$_2$O$_3$. The highlighted unit cell in the blue rectangular perfectly matches those in (d) and (e). (g) The peak intensity of the atom columns marked by the red rectangular in (d) and (e). The yellow dots are the experimental data, which agrees well with the simulated light blue line.

To study the magnetic properties of ε-Fe$_2$O$_3$ nanosheets,

temperature-dependent (M–T) and field-dependent (M–H) magnetization measurements were employed. In the M–T curves (Fig. 3(a)), the ε-Fe$_2$O$_3$ nanosheets exhibit a slight decrease of magnetization until 350 K in the field cool procedure (FC). There are also two kinks in the curve measured in the FC procedure, which is similar to that of their nanoparticle counterparts.[22,29,30] The two kinks correspond to two magnetic transitions, the one around 160 K involves the direction change of the magnetic easy axis, and the other around 133 K is related to a decrease of the coercive field. In the M–H curves under different temperatures (Fig. 3(b)), the ε-Fe$_2$O$_3$ nanosheets exhibit a well-defined hysteresis loop at 300 K, indicating ferrimagnetic properties at room temperature.[22] The magnetic force microscopy (MFM) image on a single ε-Fe$_2$O$_3$ nanosheet shows a uniform phase contrast, indicating a single domain structure at room temperature (Fig. 3(c)).

The high-quality ultrathin ε-Fe$_2$O$_3$ nanosheets with room-temperature ferrimagnetic properties can be a good candidate for exploring the magnetic proximity effect. Therefore, we constructed ε-Fe$_2$O$_3$/NbSe$_2$ heterojunctions to get further insight into magnetic proximity on superconductivity. The ultrathin ε-Fe$_2$O$_3$ nanosheet has an energy gap of about 1.9 eV, consistent with its nanoparticle counterpart.[19] Although ε-Fe$_2$O$_3$ is a non-layered material, the as-synthesized ε-Fe$_2$O$_3$ nanosheets and the mica substrate are weakly bonded.[23] Therefore, the nanosheets can be easily transferred by a standard water-assisted method. NbSe$_2$ is a van der Waals layered type-II superconductor,[31–33] which can be exfoliated into few layers to form a magnet/superconductor heterojunction with ε-Fe$_2$O$_3$ nanosheets. As the resistance of the NbSe$_2$ multilayer is much smaller than that of the ε-Fe$_2$O$_3$ nanosheet, the cur-

rent in this device can be considered to flow mainly through the NbSe$_2$ layer. To realize a precise comparison of the superconducting properties in the ε-Fe$_2$O$_3$/NbSe$_2$ heterojunction and the NbSe$_2$ multilayer, we designed a two-channel device structure on one NbSe$_2$ multilayer. As shown in Fig. 3(d), a NbSe$_2$ multilayer with uniform thickness was transferred on a group of pre-deposited parallel bottom electrodes, and then the ε-Fe$_2$O$_3$ nanosheet with a thickness of about 10 nm was stacked only on the right four electrodes to construct the ε-Fe$_2$O$_3$/NbSe$_2$ heterojunction. The electrical transport properties of the NbSe$_2$ multilayer and the ε-Fe$_2$O$_3$/NbSe$_2$ heterojunction were measured in two separate channels. The R–T curves of the NbSe$_2$ multilayer and the ε-Fe$_2$O$_3$/NbSe$_2$ heterojunction show that their critical temperatures (T_c) are 6.39 K and 6.38 K (Fig. 3(e)). The almost unchanged T_c in the heterojunction is because the in-plane magnetic moments of ε-Fe$_2$O$_3$ nanosheets generate little stray field penetrating

the NbSe$_2$ multilayer.[34] The resistance dependence of out-of-plane fields (R–$H_\perp$ curves) was also measured at different temperatures. The temperature-dependent upper critical fields ($H_{c2}^\perp$–T) were extracted and fitted with the linear 2D Ginzburg–Landau model[35]

$$\mu_0 H_{c2}^\perp(T) = \frac{\Phi_0}{2\pi\xi_{GL}^2}\left(1 - \frac{T}{T_c}\right),$$

where Φ_0 is the quantum flux and ξ_{GL} is the in-plane superconducting coherent length. The in-plane orbit-limiting pair breaking fields of the NbSe$_2$ multilayer and the ε-Fe$_2$O$_3$/NbSe$_2$ heterojunction are determined to be 5.68 T and 5.54 T from the extrapolation of $H_{c2}^\perp$ at 0 K. And the superconducting coherent lengths are calculated as 7.62 nm and 7.71 nm for the NbSe$_2$ multilayer and the heterojunction, respectively.
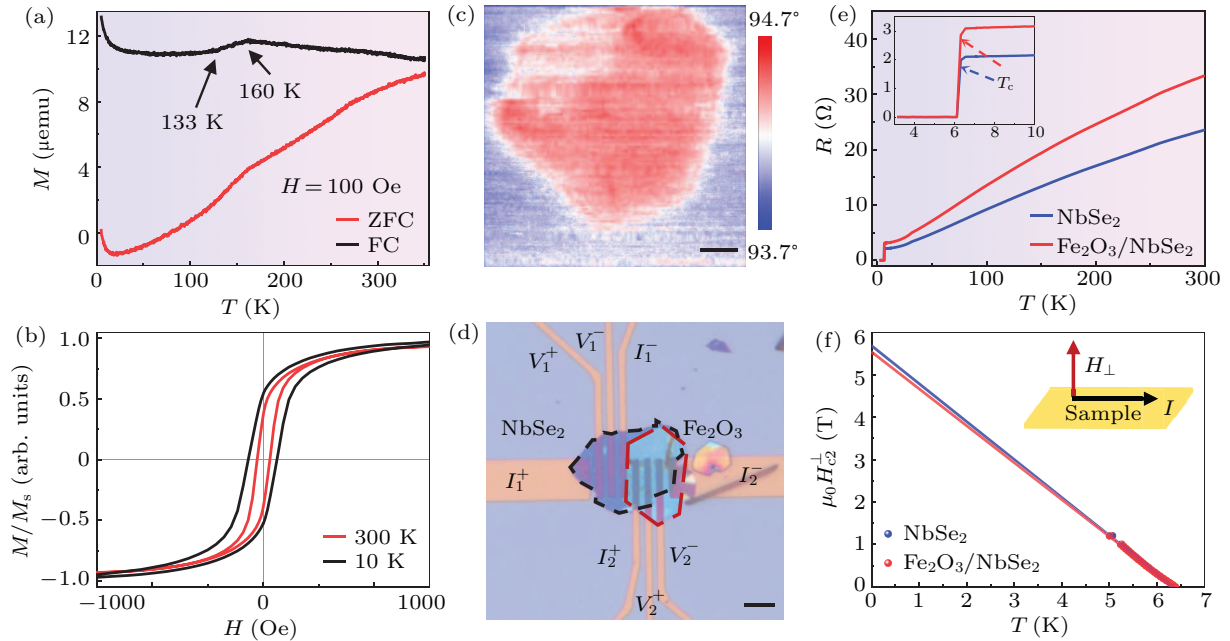
Fig. 3. Magnetic properties of ε-Fe$_2$O$_3$ nanosheets and the superconductivity of the ε-Fe$_2$O$_3$/NbSe$_2$ heterojunction. (a), (b) Temperature-dependent and field-dependent curves of ε-Fe$_2$O$_3$ nanosheets. (c) The MFM image of a typical ε-Fe$_2$O$_3$ nanosheet, indicating the uniform magnetic state. (d) The optical image of the ε-Fe$_2$O$_3$/NbSe$_2$ heterojunction device. (e) The R–T curves of the NbSe$_2$ multilayer and the ε-Fe$_2$O$_3$/NbSe$_2$ heterojunction. The inset is the R–T curves from 3 K to 10 K. T_c is defined as the temperature where the resistance reaches 90% of the normal resistance at 7 K. (f) The linear fittings for the out-of-plane upper critical magnetic fields ($H_{c2}^\perp$–T) of the NbSe$_2$ multilayer and the ε-Fe$_2$O$_3$/NbSe$_2$ heterojunction. H_{c2} is defined as the field where the resistance reaches 90% of the normal resistance. The scale bars in (c) and (d) are 0.5 μm and 5 μm.

The resistance dependence of the in-plane field (R–$H_\parallel$ curves) at different temperatures was also studied. Small humps are observed near the upper critical fields of the superconducting transition of the ε-Fe$_2$O$_3$/NbSe$_2$ heterojunction at high magnetic fields, while such a feature does not exist in the NbSe$_2$ multilayer (Figs. 4(a) and 4(b)). The humps are probably induced by the flow of Josephson vortices. The applied in-plane fields will induce interlayer Josephson vortices in the NbSe$_2$ multilayer, which penetrate the ε-Fe$_2$O$_3$ nanosheet. Since the vortices are weakly pinned in the ε-

Fe$_2$O$_3$ nanosheet, when a current perpendicular to the field flows through them, the vortices can be de-pinned and driven by the Lorentz force. The collective movement of the Josephson vortices leads to large energy dissipation and results in a limited magnetoresistance.[36,37] The $H_{c2}^\parallel$–T curves were also plotted and fitted with in-plane 2D Ginzburg–Landau model[35]

$$\mu_0 H_{c2}^\parallel(T) = \frac{\Phi_0\sqrt{12}}{2\pi\xi_{GL}d_{SC}}\sqrt{1 - \frac{T}{T_c}},$$

where d_{SC} is the effective thickness of the superconductor.

The superconducting effective thicknesses can be obtained to be 8.53 nm and 8.94 nm for the NbSe$_2$ multilayer and the ε-Fe$_2$O$_3$/NbSe$_2$ heterojunction. Thus, the obtained T_c, H_{c2}, ξ_{GL} and d_{SC} in the NbSe$_2$ multilayer and ε-Fe$_2$O$_3$/NbSe$_2$ heterojunction are concluded nearly the same.

Besides T_c and H_{c2}, the critical supercurrent (I_c) is another important parameter for a superconductor. Therefore, V–I curves for both the NbSe$_2$ multilayer and the ε-Fe$_2$O$_3$/NbSe$_2$ heterojunction were also measured to study the magnetic proximity effect on superconducting properties. Although the I_c is nearly the same at about 0.45 mA for both the NbSe$_2$ multilayer and the ε-Fe$_2$O$_3$/NbSe$_2$ heterojunction, the transition from the superconducting state to normal state (ΔI) is different (Fig. 4(d)). The ΔI for the heterojunction is much larger than that for the NbSe$_2$ multilayer, which might result from the interaction between the magnetic moment of the ε-Fe$_2$O$_3$ nanosheet and the magnetic flux generated by the current in the NbSe$_2$ multilayer.[38] The V–I measurements were also carried out under different out-of-plane magnetic fields. The field-dependent critical currents I_c^+ (I_c^-) at a positive (negative) bias were extracted from the V–I curves. A field-induced nonreciprocal charge transport for the NbSe$_2$ multilayer was observed (Fig. 4(e)), which is significantly suppressed in the ε-Fe$_2$O$_3$/NbSe$_2$ heterojunction (Fig. 4(f)). The nonreciprocal critical current under positive and negative bias originates from the valley-Zeeman spin–orbit interaction (SOI) of NbSe$_2$.[39,40] In NbSe$_2$ few layers, the electron spin is locked with valleys in the out-of-plane direction.[41] When an out-of-plane field is applied, the degeneracy of valleys with opposite momenta is broken by the Zeeman effect, which will possibly induce asymmetric pinning potentials in the NbSe$_2$ multilayer.[42] And the collective flow of the vortices in the NbSe$_2$ multilayer driven by the external charge current among these asymmetric pinning potentials will cause nonreciprocal transport behavior.[40,43] This phenomenon is suppressed under high fields, similar to the previously reported results.[40,44–47] In the heterojunction, the ε-Fe$_2$O$_3$ nanosheet on top of the NbSe$_2$ multilayer might generate a complex pinning effect that competes with the asymmetric pinning potentials generated by the valley-Zeeman SOI in NbSe$_2$ to interference the vortex flow, and therefore suppresses the nonreciprocal transport behavior. The results indicate that the strong SOI exists at the interface between the nonlayered ε-Fe$_2$O$_3$ nanosheet and the NbSe$_2$ multilayer, and prove that the ε-Fe$_2$O$_3$ nanosheets are smooth and clean enough to construct 2D heterojunctions.
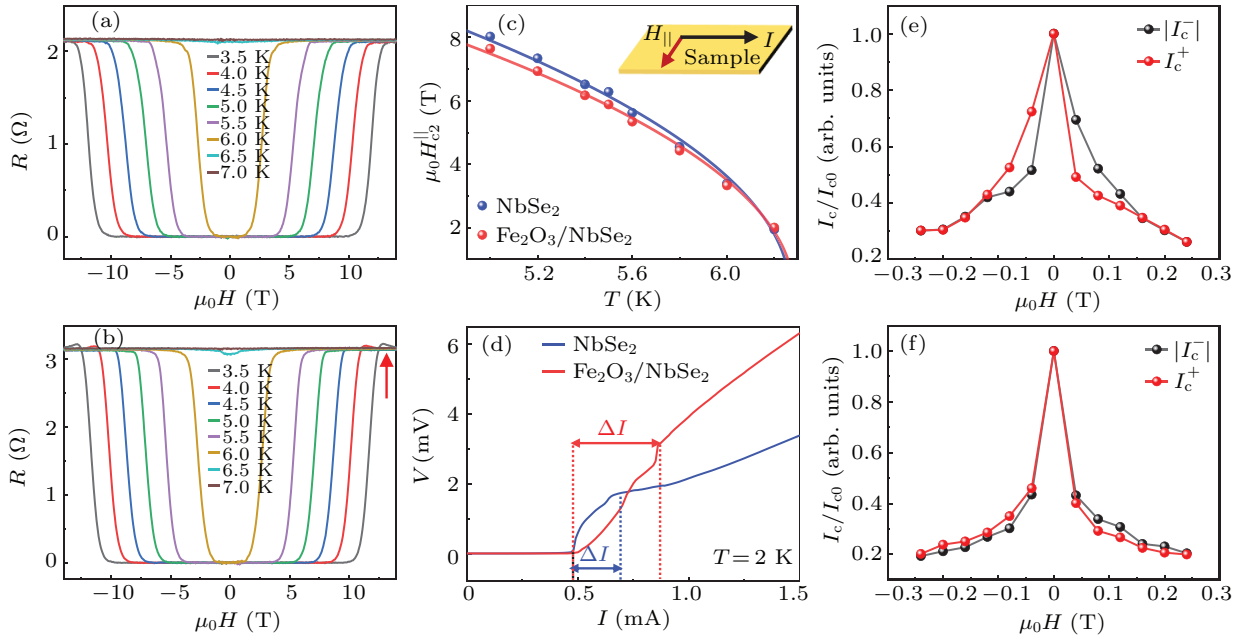
Fig. 4. Electrical transport properties of the NbSe$_2$ multilayer and the ε-Fe$_2$O$_3$/NbSe$_2$ heterojunction. (a), (b) The R–H curves of the NbSe$_2$ and the ε-Fe$_2$O$_3$/NbSe$_2$ heterojunction regions. The red arrow in (b) indicates the hump which appears near $H_{c2}^{\parallel}$ at high fields. (c) The fitting curves for in-plane $H_{c2}^{\parallel}$–T of the NbSe$_2$ multilayer and the ε-Fe$_2$O$_3$/NbSe$_2$ heterojunction. (d) The V–I curves of the NbSe$_2$ multilayer and the ε-Fe$_2$O$_3$/NbSe$_2$ heterojunction at 2 K. ΔI is the current range of superconducting transition. (e), (f) The out-of-plane magnetic field-dependent positive and negative I_c extracted from the V–I curves of the NbSe$_2$ multilayer and the ε-Fe$_2$O$_3$/NbSe$_2$ heterojunction.

4. Conclusion

We successfully synthesized high-quality ε-Fe$_2$O$_3$ nanosheets by a space-confined CVD method and verified its high crystalline quality by STEM characterization. The magnetic measurements show that the ε-Fe$_2$O$_3$ nanosheets remain ferrimagnetic up to 350 K. An ultrathin ε-Fe$_2$O$_3$ nanosheet was used to construct the ε-Fe$_2$O$_3$/NbSe$_2$ heterojunction to study the magnetic proximity effect on superconductivity of NbSe$_2$ multilayer. The electrical transport results demonstrate that the T_c, H_{c2} and I_c in the NbSe$_2$ multilayer and

ε-Fe$_2$O$_3$/NbSe$_2$ heterojunction are nearly the same, indicating that the ε-Fe$_2$O$_3$ nanosheet has a minor influence on the superconductivity of the NbSe$_2$ multilayer. However, the proximity effect of the ε-Fe$_2$O$_3$ nanosheet shows an obvious modulation effect on the interfacial SOI, which suppresses the nonreciprocal transport of the NbSe$_2$ multilayer. This work shows that non-layered ferrimagnetic ε-Fe$_2$O$_3$ nanosheets can form 2D heterojunctions with other 2D vdW materials to modulate their properties by proximity effect, which enables the ε-Fe$_2$O$_3$ nanosheets and further non-layered 2D magnets with stronger perpendicular anisotropy[48] to be potential building blocks for spintronics and superconducting spintronic devices.

Acknowledgements

References

[1] Lee C, Katmis F, Jarillo-Herrero P, Moodera J S and Gedik N 2016 *Nat. Commun.* **7** 12014
[2] Katmis F, Lauter V, Nogueira F S, Assaf B A, Jamer M E, Wei P, Satpati B, Freeland J W, Eremin I, Heiman D, Jarillo-Herrero P and Moodera J S 2016 *Nature* **533** 513
[3] MacDonald A H, Schiffer P and Samarth N 2005 *Nat. Mater.* **4** 195
[4] Zhong D, Seyler K L, Linpeng X, Cheng R, Sivadas N, Huang B, Schmidgall E, Taniguchi T, Watanabe K, McGuire M A, Yao W, Xiao D, Fu K C and Xu X 2017 *Sci. Adv.* **3** e1603113
[5] Seyler K L, Zhong D, Huang B, Linpeng X, Wilson N P, Taniguchi T, Watanabe K, Yao W, Xiao D, McGuire M A, Fu K M and Xu X 2018 *Nano Lett.* **18** 3823
[6] Zhao C, Norden T, Zhang P, Zhao P, Cheng Y, Sun F, Parry J P, Taheri P, Wang J, Yang Y, Scrace T, Kang K, Yang S, Miao G X, Sabirianov R, Kioseoglou G, Huang W, Petrou A and Zeng H 2017 *Nat. Nanotechnol.* **12** 757
[7] Buzdin A I 2005 *Rev. Mod. Phys.* **77** 935
[8] Bergeret F S, Volkov A F and Efetov K B 2005 *Rev. Mod. Phys.* **77** 1321
[9] Eschrig M 2015 *Reports on Progress in Physics* **78** 104501
[10] Beenakker C W J 2013 *Annual Review of Condensed Matter Physics* **4** 113
[11] Aikebaier F, Heikkilä T T and Lado J L 2022 *Phys. Rev. B* **105** 054506
[12] Yao Y, Zhan X, Sendeku M G, Yu P, Dajan F T, Zhu C, Li N, Wang J, Wang F, Wang Z and He J 2021 *Nanotechnology* **32** 472001
[13] McGuire M A, Dixit H, Cooper V R and Sales B C 2015 *Chemistry of Materials* **27** 612
[14] Dillon J F and Olson C E 1965 *J. Appl. Phys.* **36** 1259
[15] Gong C, Li L, Li Z, Ji H, Stern A, Xia Y, Cao T, Bao W, Wang C, Wang Y, Qiu Z Q, Cava R J, Louie S G, Xia J and Zhang X 2017 *Nature* **546** 265
[16] Deng Y, Yu Y, Song Y, Zhang J, Wang N Z, Sun Z, Yi Y, Wu Y Z, Wu S, Zhu J, Wang J, Chen X H and Zhang Y 2018 *Nature* **563** 94
[17] Zhao B, Ngaloy R, Ghosh S, Ershadrad S, Gupta R, Ali K, Hoque A M, Karpiak B, Khokhriakov D, Polley C, Thiagarajan B, Kalaboukhov A, Svedlindh P, Sanyal B and Dash S P 2023 *Adv. Mater.* **35** 2209113

[18] May A F, Ovchinnikov D, Zheng Q, Hermann R, Calder S, Huang B, Fei Z, Liu Y, Xu X and McGuire M A 2019 *ACS Nano* **13** 4436
[19] Cornell R M and Schwertmann U 2003 *The iron oxides: structure, properties, reactions, occurrences, and uses* (Weinheim: Wiley-vch) pp. 111–137
[20] Kelm K and Mader W 2005 *Z. Anorg. Allg. Chem.* **631** 2383
[21] Gich M, Frontera C, Roig A, Taboada E, Molins E, Rechenberg H R, Ardisson J D, Macedo W A A, Ritter C, Hardy V, Sort J, Skumryev V and Nogués J 2006 *Chemistry of Materials* **18** 3889
[22] Tuček J, Zbořil R, Namai A and Ohkoshi S I 2010 *Chemistry of Materials* **22** 6483
[23] Yuan J, Balk A, Guo H, Fang Q, Patel S, Zhao X, Terlier T, Natelson D, Crooker S and Lou J 2019 *Nano Lett.* **19** 3777
[24] Wang Y, Wang P, Wang H, Xu B, Li H, Cheng M, Feng W, Du R, Song L, Wen X, Li X, Yang J, Cai Y, He J, Wang Z and Shi J 2023 *Adv. Mater.* **35** 2209465
[25] Zhao Z, Fang Z, Han X, Yang S, Zhou C, Zeng Y, Zhang B, Li W, Wang Z, Zhang Y, Zhou J, Zhou J, Ye Y, Hou X, Zhao X, Gao S and Hou Y 2023 *Nat. Commun.* **14** 958
[26] Liu S, Wang S, Guo J and Guo Q 2012 *RSC Advances* **2** 9938
[27] Xue M, Wang S, Wu K, Guo J and Guo Q 2011 *Langmuir* **27** 11
[28] López-Sánchez J, Serrano A, Del Campo A, Abuín M, Rodríguez de la Fuente O and Carmona N 2016 *Chemistry of Materials* **28** 511
[29] Gich M, Roig A, Frontera C, Molins E, Sort J, Popovici M, Chouteau G, Martín y Marero D and Nogués J 2005 *J. Appl. Phys.* **98** 044307
[30] Sakurai S, Jin J, Hashimoto K and Ohkoshi S I 2005 *J. Phys. Soc. Jpn.* **74** 1946
[31] Frindt R F 1972 *Phys. Rev. Lett.* **28** 299
[32] Dvir T, Massee F, Attias L, Khodas M, Aprili M, Quay C H L and Steinberg H 2018 *Nat. Commun.* **9** 598
[33] Ugeda M M, Bradley A J, Zhang Y, Onishi S, Chen Y, Ruan W, Ojeda-Aristizabal C, Ryu H, Edmonds M T, Tsai H-Z, Riss A, Mo S K, Lee D, Zettl A, Hussain Z, Shen Z X and Crommie M F 2016 *Nat. Phys.* **12** 92
[34] Ahamed I, Pathak R, Skomski R and Kashyap A 2018 *AIP Advances* **8** 055815
[35] Tinkham M and Emery V 1996 *Physics Today* **49** 74
[36] Uji S, Terashima T, Nishimura M, Takahide Y, Konoike T, Enomoto K, Cui H, Kobayashi H, Kobayashi A, Tanaka H, Tokumoto M, Choi E S, Tokumoto T, Graf D and Brooks J S 2006 *Phys. Rev. Lett.* **97** 157001
[37] Jiang D, Yuan T, Wu Y, Wei X, Mu G, An Z and Li W 2020 *ACS Applied Materials & Interfaces* **12** 49252
[38] Khanukov A, Mangel I, Wissberg S, Keren A and Kalisky B 2022 *Phys. Rev. B* **106** 144510
[39] He J J, Tanaka Y and Nagaosa N 2022 *New J. Phys.* **24** 053014
[40] Bauriedl L, Bäuml C, Fuchs L, Baumgartner C, Paulik N, Bauer J M, Lin K Q, Lupton J M, Taniguchi T, Watanabe K, Strunk C and Paradiso N 2022 *Nat. Commun.* **13** 4266
[41] Xi X, Wang Z, Zhao W, Park J H, Law K T, Berger H, Forró L, Shan J and Mak K F 2016 *Nat. Phys.* **12** 139
[42] Zhang E, Xu X, Zou Y C, Ai L, Dong X, Huang C, Leng P, Liu S, Zhang Y, Jia Z, Peng X, Zhao M, Yang Y, Li Z, Guo H, Haigh S J, Nagaosa N, Shen J and Xiu F 2020 *Nat. Commun.* **11** 5634
[43] Hoshino S, Wakatsuki R, Hamamoto K and Nagaosa N 2018 *Phys. Rev. B* **98** 054510
[44] Ando F, Miyasaka Y, Li T, Ishizuka J, Arakawa T, Shiota Y, Moriyama T, Yanase Y and Ono T 2020 *Nature* **584** 373
[45] Baumgartner C, Fuchs L, Costa A, Reinhardt S, Gronin S, Gardner G C, Lindemann T, Manfra M J, Faria Junior P E, Kochan D, Fabian J, Paradiso N and Strunk C 2022 *Nat. Nanotechnol.* **17** 39
[46] Yuan N F Q and Fu L 2022 *Proc. Natl. Acad. Sci. USA* **119** e2119548119
[47] Ilić S and Bergeret F 2022 *Phys. Rev. Lett.* **128** 177001
[48] Bian M, Zhu L, Wang X, Choi J, Chopdekar R V, Wei S, Wu L, Huai C, Marga A, Yang Q, Li Y C, Yao F, Yu T, Crooker S A, Cheng X M, Sabirianov R F, Zhang S, Lin J, Hou Y and Zeng H 2022 *Adv. Mater.* **34** 2200117